Research paper

Co/N−C nanotubes with increased coupling sites by space-confined pyrolysis for high electrocatalytic activity

Jun Yang [a], Laiquan Li [a], Hong Yu [b], Hongbo Geng [b], Chengchao Li [b,**], Xiaochen Dong [a,*]

[a] *Key Laboratory of Flexible Electronics (KLOFE) & Institute of Advanced Materials (IAM), Jiangsu National Synergetic Innovation Center for Advanced Materials (SICAM), Nanjing Tech University (NanjingTech), 30 South Puzhu Road, Nanjing 211816, China*
[b] *School of Chemical Engineering and Light Industry, Guangdong University of Technology, Guangzhou 510006, China*

Abstract

Searching low cost and non-precious metal catalysts for high-performance oxygen reduction reaction is highly desired. Herein, Co nanoparticles embedded in nitrogen-doped carbon (Co/N−C) nanotubes with internal void space are successfully synthesized by space-confined pyrolysis, which effectively improve the cobalt loading content and restrict the encapsulated particles down to nanometer. Different from the typical conformal carbon encapsulation, the resulting Co/N−C nanotubes possess more cobalt nanoparticles embedded in the nanotubes, which can provide more coupling sites and active sites in the oxygen reduction reaction (ORR). Moreover, the one-dimensional and porous structure provides a high surface area and a fast electron transfer pathway for the ORR. And the Co/N−C electrode presents excellent electrocatalytic ORR activity in terms of low onset potential (30 mV lower than that of Pt/C), small Tafel slop (45.5 mV dec^{-1}) and good durability (88.5% retention after 10,000 s).

1. Introduction

The oxygen reduction reaction (ORR) attracts great attention due to its crucial role in renewable energy technologies including metal-air batteries [1−3] and fuel cells [4−6]. Tremendous efforts have been made to develop oxygen electrode catalysts with high activity and low cost. Currently, platinum (Pt) or its alloys are the most active catalysts in facilitating the rate of ORR. However, they still suffer from high cost and declining activity under fuel cell conditions [7]. Thus, lots of researches have been focused on developing non-precious metals and metal free materials as alternative catalysts [8,9]. On the other hand, a great deal of non-precious materials has even better ORR performance in alkaline solution than in acid medium due to the higher electrode reaction kinetics. In addition, the fuel cell performance may be improved by the alkaline anion-exchange membranes and the alkaline media offers a less corrosive environment to the electrodes [10]. Thus, a large spectrum of effective and inexpensive non-platinum electrocatalysts in alkaline medium have sparked over the past decade [11−14].

Recently, transition metal based materials have attracted great attention in the field of electro-catalysis [15−17], especially the transition metal nanoparticles (e.g., Ni, Fe, Co) encapsulated in carbon materials have emerged as potential substitutes for Pt and other precious metals due to their low cost and attracted broad interest as electrocatalytic materials [18−21]. The enhanced chemical activities of transition metal/ carbon electrocatalysts are believed to be related to the

* Corresponding author.
** Corresponding author.
E-mail addresses: licc@gdut.edu.cn (C. Li), iamxcdong@njtech.edu.cn (X. Dong).

interaction between metallic nanoparticles and carbon materials [22]. The introduction of transition metal/metal oxide may optimize the local work function and electronic structure of the carbon materials and afford high catalytic activity by synergistic effect [23]. To this end, great efforts have been dedicated to developing nano-structured transition metal/carbon composite electrocatalyst [8,24]. However, the corrosion feature and poor stability of the transition metals or derivatives result in poor performances during the measurement [25]. Encapsulation the particles with functional carbonous materials provides an effective approach for enhancing electrocatalytic activity and stability [26,27]. The hybridizing strategy has been demonstrated on the synthesis of Co/nitrogen-rich carbon tubes [28], Mn−Co oxide/carbon tubes [29], Co/graphene shells [30], and so on. These catalysts delivered high performance towards the OER, HER or ORR with improved stability. However, the transition metal/carbon electrocatalysts are mostly synthesized by pyrolizing precursor mixtures containing organic components and transition metal salts. The content of transition metals in the eletrocatalysts is very low, which leads to limited coupling effect and site density. It is suggested that the content and dispersity of transition metal as well as their interphase structure with carbon materials are keys to the complex electrocatalysts [31,32]. Though, electrostatic spinning of metal-coordinating carbon materials can increase the content of the metal, the metal core inside the carbon is not porous, which makes the sample lack active sites in ORR performance [28]. Thus, it is still a challenge to improve the catalytic performance by increasing coupling sites between carbon and transition metals.

In addition, morphology and porosity of the catalyst are the other key factors affecting their electrocatalytic efficiency. Many kinds of porous materials have been synthesized to be used for ORR, which can provide large surface areas, multidimensional electron transport pathways, interfacial transport, and shorter diffusion paths or reduce the diffusion effect [33]. Unfortunately, most of carbon-encapsulated metal nanoparticle electrocatalyts are conformal carbon layer, which is unfavorable for ion and electron transport [34]. In spite of the great potentials for ORR, few reports have shown excellent activity and durability in comparison with commercial Pt/C catalysts. Therefore, it is highly desired to develop a convenient, scalable and economical approach to prepare porous carbon-encapsulated transition metal with improved content and dispersity.

Herein, Co/N-carbon nanotubes were synthesized by integration of surface coating and space-confined pyrolysis process. First, cobalt coordination polymer nanowires (CPNs) were hydrothermal synthesized through co-precipitation. Then, dopamine was used to get Co coordination polymer/polydopamine core/shell nanowires. Finally, the Co/N-doped carbon (Co/N−C) nanotubes can be obtained by thermal annealing in hydrogen gas. In contrast to the traditionally conformal carbon coating, the Co nanoparticles inside the carbon nanotubes have a large void space, which provides large Brunauer−Emmett−Teller (BET) surface area

(204.3 m^2 g^{-1}) for fast electrolyte diffusion in ORR. Moreover, the increased cobalt nanoparticles-carbon coupling sites will greatly improve the catalytic activity for ORR performance. Specifically, the Co/N−C electrode demonstrates comparable oxygen reduction reaction catalytic activity with commercial Pt/C in terms of low onset potential (30 mV lower than that of the Pt/C), small Tafel slop (45.5 mV dec^{-1}) and good durability (88.5% retention after 10000 s).

2. Experimental section

2.1. Synthesis of coordination polymer nanowires

Typically, $CoCl_2$ (1.2 g) and nitrilotriacetic acid (0.6 g) were added into 40 mL mixed solvent of deionized (DI) water and isopropyl alcohol with vigorous stirring. The mixture was then transferred into a Teflon-lined autoclave, which was heated gradually to 180 °C and maintained for 12 h. The pink products were collected by centrifugation and washed with water and ethanol for several times, drying at 60 °C for 12 h in oven.

2.2. Synthesis of Co/N−C nanotubes

A certain amount of Co-based coordination polymer nanowires was dispersed in 10 mM tris buffer (pH = 8.5) with the assistance of ultrasonication. Then, 2 mL DI water containing 160 mg dopamine was added into the mixture under vigorous stirring. After 48 h, the black product was collected by centrifugation and washed with ethanol for three times and dried at 60 °C for 12 h in oven. The dried sample was further annealed at 800 °C for 4 h with a heating rate of 10 °C min^{-1} in forming gas (5% H_2, 95% Ar).

2.3. Electrochemical measurements

The electrochemical characterization was carried out in 1.0 M KOH solution using a CHI 760E electrochemical workstation (CHI Inc., USA). The three-electrode cell consisted of a Pt counter-electrode, an Ag/AgCl reference electrode, and a glassy carbon modified with various catalysts as a working electrode. The working electrode were prepared as follows: 5.0 mg of the sample was mixed with 1.0 mg of carbon black, Nafion solution (5.0% Nafion in ethanol, 50 μL), DI water, (475 μL) and ethanol (475 μL). The mixture was sonicated for 30 min and 10.0 μL suspension was dropped onto the glassy carbon electrode (diameter 5 mm) and dried for 6 h. All potentials were referenced against the reversible hydrogen electrode (RHE) base on the Nernst equation ($E_{RHE} = E_{Ag/AgCl} + 0.059 \times pH + 0.197$ V). Before electrochemical tests, the working electrode was first kept in an Ar-saturated electrolyte by cycling in the potential range of 0.1−1.2 V at a scan rate of 100 mV s^{-1} until reproducible cyclic voltammograms were obtained. After that, the oxygen saturated electrolyte was characterized and recorded for oxygen reduction in the potential range of 0.1−1.2 V at a scanning rate of 5−100 mV s^{-1}. For comparison, the commercial Pt/C

catalyst (HP 10% Platinum on Vulcan XC-72 1 g, Fuel Cell Store) was also performed under the same conditions. The mass loading of each electrode is about 0.26 mg cm^{-2}.

2.4. Characterization

X-ray powder diffraction (XRD) (Bruker AXS D8) was carried out using Cu Kα radiation. Morphology of the samples was investigated using a field emission scanning electron microscope (FESEM, JEOL, Model JSM-7600F). TEM characterization was performed with a JEOL 2100F operated at 200 kV. The nitrogen adsorption/desorption isotherms were obtained by an accelerated surface area and porosimetry system (ASAP 2020) at 196 °C. And the specific surface areas were calculated by using the BET method. X-ray photoelectron spectroscopy (XPS) was performed by AXIS-His (Kratos Analytical). TGA analysis of the samples was conducted on Mettler Toledo TGA/DSC1 Simultaneous Thermal Analyzer in air. The temperature was programmed to rise from 25 to 800 °C at 10 °C min^{-1}.

3. Results and discussion

A diagram describing the synthesis of Co/N−C nanotubes is schematically illustrated in Fig. 1. Initially, the cobalt coordination polymer nanowires, obtained from the hydrothermal step, were coated with polydopamine through immersion of the sample in an aqueous solution of dopamine. It was proved recently that dopamine can self-polymerize at alkaline pH values and spontaneously deposit on virtually any surface to form conformal films [35−37]. Specifically, the catechol and amine functional groups of dopamine presented a strong binding affinity to the surface of Co coordination polymer nanowires, and the dopamine can be transformed into 5,6-dihydroxyindole through oxidization and cyclization process. After that, it will self-polymerize in buffer and deposit to form continuous polydopamine films on the surface of Co coordination polymer nanowires [38]. Subsequently, the core−shell structure Co coordination polymer/polydopamine was transformed into Co/N−C nanocomposites by annealing at 800 °C under H$_2$/Ar (5:95 v/v) atmosphere. Fig. 2a and b show the SEM and TEM images of Co coordination polymer at different magnifications, revealing that all Co coordination polymer presents nanowire morphology with uniform size distribution and open ends. Each Co coordination polymer possesses an average diameter of 50 nm and a length of about 20 μm.

Fig. 3a shows the XRD patterns of Co/N−C nanotubes. As can be seen, all the diffraction peaks can be indexed to the cubic Co (JCPDS card no. 15-0806). Three characteristic peaks of Co/N−C (2θ = 44.26°, 51.57°, 75.93°) can be observed, corresponding to the (111), (200) and (220) planes. After heat treatment process, the SEM images of Co/N−C nanotubes in Fig. 3b and c indicate that nanowire morphology was well reserved with the rougher surface. Fig. 3d and e show the typical TEM image of Co/N−C nanotubes. It can be clearly seen that large amount of Co nanoparticles with the average of 10 nm are dispersed inside the carbon nanotubes with the diameter of 70 nm. Moreover, more than 50% void
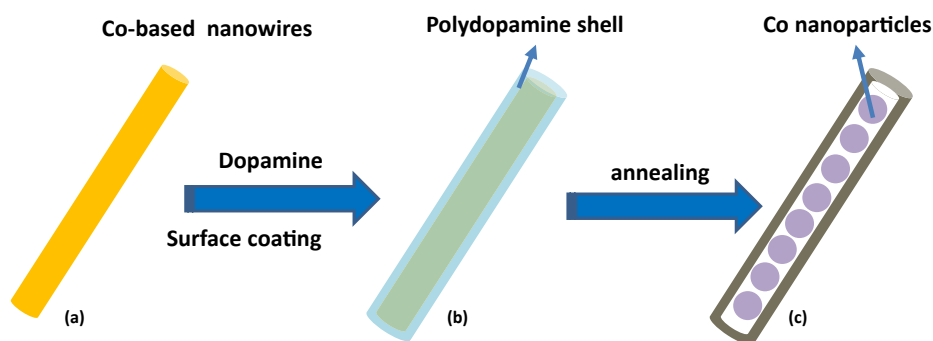

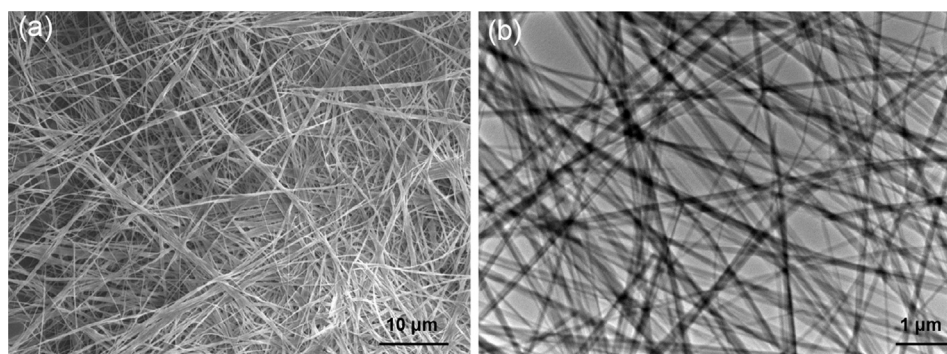Fig. 1. Schematic illustration on the preparation of Co/N−C nanotube.

Fig. 2. (a) SEM and (b) TEM image of the Co coordination polymer nanowires.
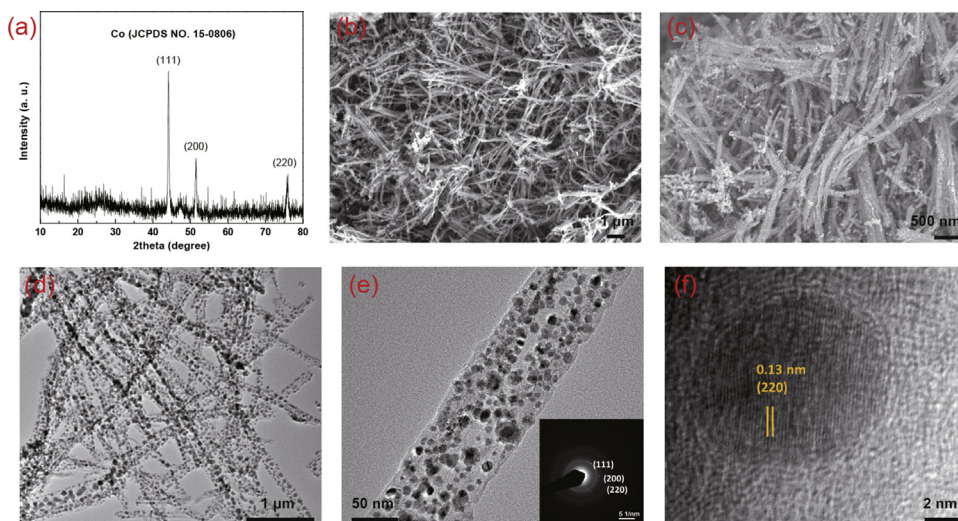
Fig. 3. (a) XRD pattern, (b, c) SEM images, (d, e) TEM images, (f) HRTEM image of Co/N−C nanotubes (Inset (e) is the corresponding SAED pattern).

space was provided, which allows for fast electron transfer and electrolyte diffusion in the ORR. The corresponding diffraction rings in the selected area electron diffraction (SAED) pattern (Inset of Fig. 3e) are composed of discontinuous concentric rings that can be identified as the (111), (200) and (220) planes of cubic Co, revealing that the nanotubes are polycrystalline. As shown in the high-resolution TEM (HRTEM) image (Fig. 3f), the highly resolved lattice fringes with an inter-planar spacing of 0.13 nm corresponds to the (220) plane of cubic-type Co.

Fig. 4a and b show the TEM image of the pure carbon nanotubes after etching treatment of the Co/N−C nanotubes in 1 M hydrochloric acid for 2 h. Porous carbon nanotubes with the average size of 70 nm can be obtained without any cobalt nanoparticles existed. It reveals that the Co nanoparticles are partially embedded in the shell of carbon nanotubes with sufficient contact, leading to low contact resistance and high electron transfer efficiency. Besides, the strong coupling between carbon and cobalt nanoparticles would be achieved, because of the intimate contact, which facilitates the high catalytic activity of the Co/N−C nanotubes.

To further probe the chemical environment and bonding configuration in the Co/N−C nanotubes, X-ray photoelectron spectroscopy (XPS) measurement (Fig. 5a and b) was carried out. In Fig. 5a, the strong peaks at 284.6 can be assigned to sp^3C-sp^3C, whereas the other two signals at 285.6 and 286.4 eV correspond to N-sp^2C and related oxidative forms (O=C−O) [39]. Similarly, the two peaks in N 1s peak (Fig. 5b) at 401.0 and 398.2 eV can be indexed to pyrrolic and pyridine N atoms, indicating the presence of a N-doped carbon matrix [40]. Fig. 5c presents the nitrogen adsorption−desorption isotherm curves of the Co/N−C sample, which indicate that the sample has a BET surface area of 204.3 m^2 g^{-1}. The pore size distribution (Fig. 5c inset) exhibits a multimodal mesopore size distribution property. The mesopores with diameters of 10−20 nm may be generated from the carbon shell by pyrolysis, and the macropores (50−60 nm) might be arising from the interspace voids between Co nanoparticles. These results are in agreement with the TEM results in Fig. 3e. Furthermore, the content of Co in the Co/N−C nanotubes was characterized by the TGA analysis. As shown in Fig. 5d, the first weight increase in the 200−260 °C range is owing to the oxidation of Co nanoparticles and the drastic weight loss (25%) in the 260−450 °C can be attributed to the carbon loss in air flow. Based on the TGA results, the calculated Co content in the sample is as high as 68.3%, which is much higher than the reported products prepared by catalytic growth route [29].
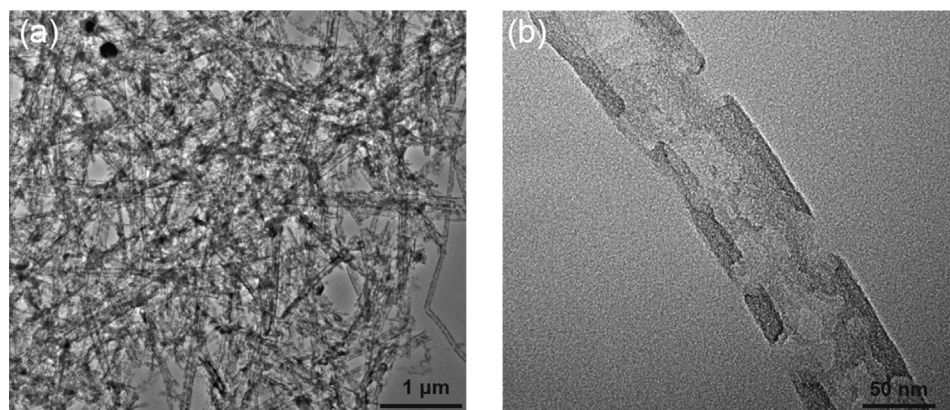

Fig. 4. (a, b) TEM images of carbon nanotubes after acid-corrosion of the Co/N−C nanotubes.
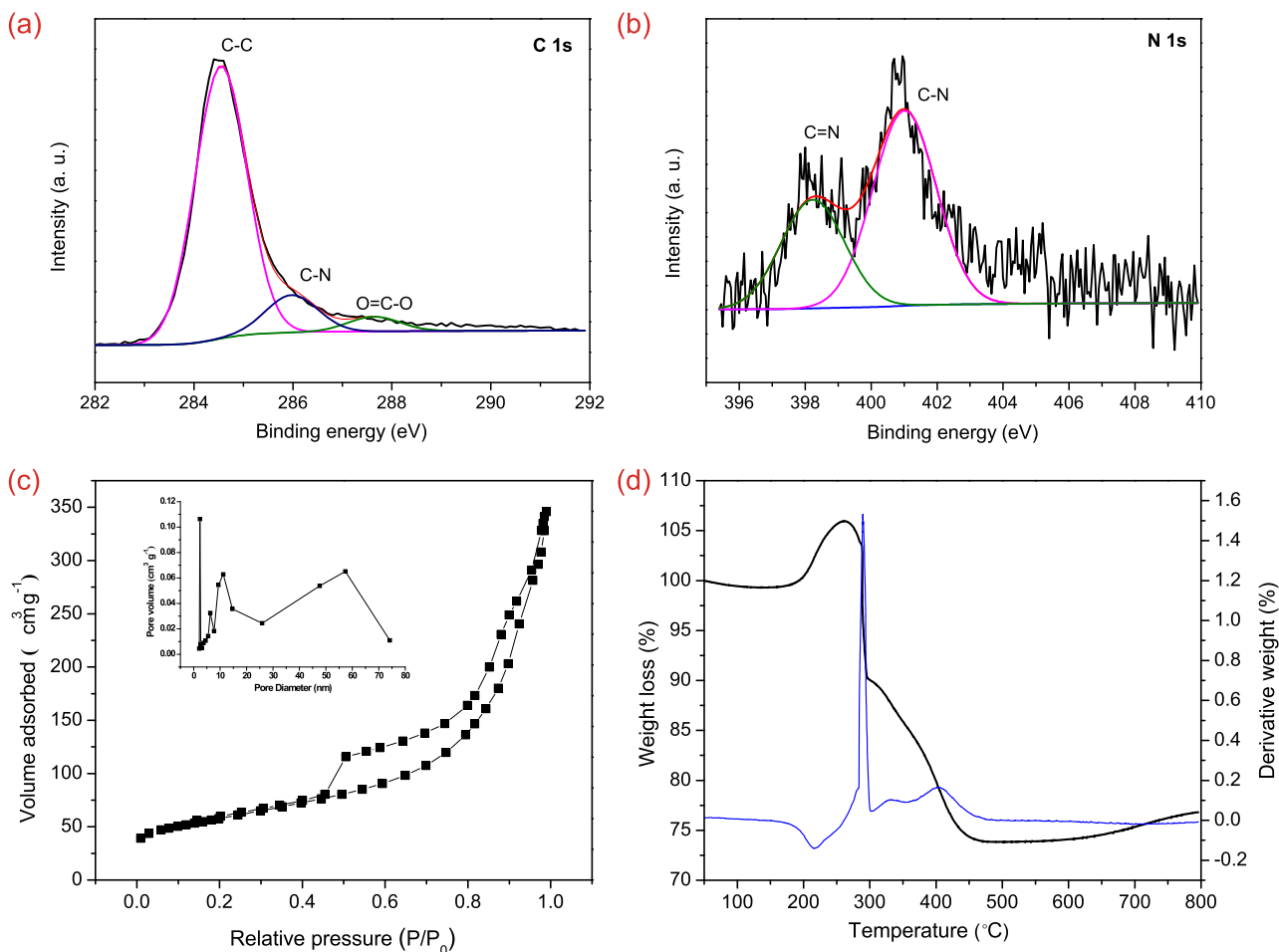
Fig. 5. (a) The high resolution C 1s XPS spectra and (b) N 1s peak in Co/N−C nanotubes. (c) N$_2$ adsorptiondesorption isotherms of Co/N−C nanotubes (The inset of (c) shows the corresponding pore size distribution curve). (d) The thermogravimetric analysis of Co/N−C nanotubes.

The ORR electrocatalytic activity of Co/N−C electrode was firstly studied through cyclic voltammetry (CV) in a 1 M KOH solution saturated with argon and oxygen. As shown in Fig. 6a, the Co/N−C electrode exhibits a well-defined reduction peak (around 0.80 V) in an O$_2$-saturated electrolyte, which is slightly less than that of the Pt/C (0.83 V). Moreover, the linear-sweep voltammograms (LSV) of the Co/N−C and Pt/C catalysts in O$_2$-saturated electrolyte at a scan rate of 10 mV s^{-1} and a rotating speed of 1600 rpm was provided in Fig. 6b. Besides, the onset potentials (0.92 V) and half-wave potential (0.87 V) of the Co/N−C are close to that of the Pt/C (0.95 V, 0.90 V). At higher over potentials, the current density of ~3.48 mA cm^{-2} for the Co/N−C and ~3.53 mA cm^{-2} for the Pt/C can be achieved. It indicates that the Co/N−C electrode shows an excellent ORR activity with a positive onset potential and a high diffusion current. The LSVs were also measured from 400 to 2025 rpm (Fig. 6c). All LSVs for Co/N−C electrode present typical increasing current with higher rotation speeds and the current density has an obvious platform. Based on the platform data, The Koucteckye Levich (K−L) plots (J^{-1} versus $w^{-0.5}$) at different potentials can be obtained, as shown in Fig. 6d. According the RDE tests and K−L theory [41,42], the electron transfer numbers (*n*) of

catalyst were calculated to be ~3.9 at 0.55−0.75 V, which reveals that a near four electron ORR pathway catalyzed by the Co/N−C. The ORR performed in alkaline electrolyte usually includes the following reactions [43]:

$$O_2 + 2H_2O + 4e^- \rightarrow 4OH^- \tag{1}$$

$$O_2 + 2H_2O + 2e^- \rightarrow H_2O_2 + 2OH^- \tag{2}$$

Fig. 6e shows the Tafel tests of the Co/N−C and Pt/C electrode. The slope of the Co/N−C (45.5 mV per decade) is much smaller than that of the Pt/C (63.9 mV per decade), which indicates that the polarization of ORR caused by the Co/N−C catalyst is lower. Durability is one of the major challenges for catalyst in alkaline fuel cells. As shown in Fig. 6f, only 11.5% current drop can be observed during the durability test in the current (I)-time (t) curves of the Co/N−C at 0.8 V, whereas the Pt/C catalyst typically shows 27.3% decrease in activity after only 10000 s in 1 M KOH. Since the Co/N−C catalyst exhibits a nearly four-electron oxygen reduction pathway for the ORR, it is not surprising that the catalyst has excellent durability. As shown in Table 1, with comparison of previous developments [30,44−49], the electrocatalyst demonstrated here is superior. The
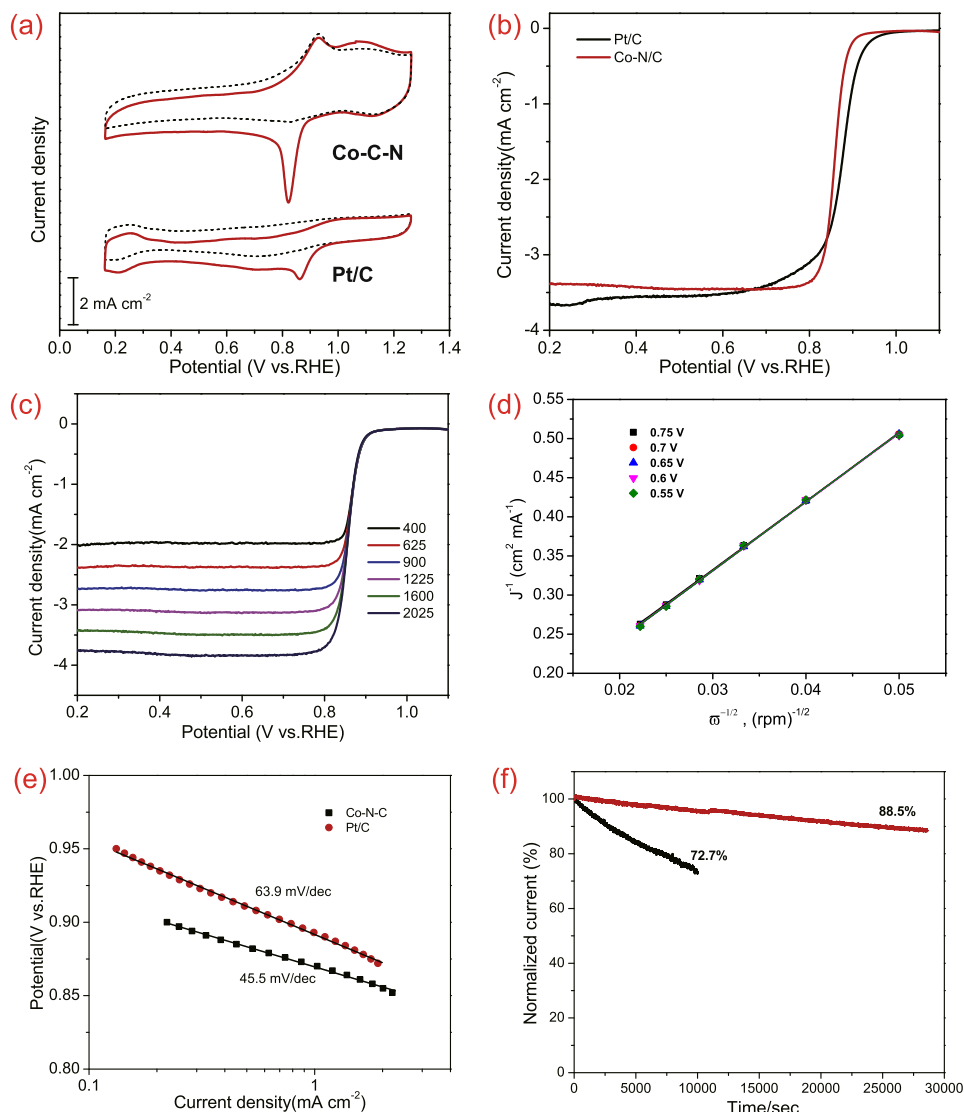
Fig. 6. (a) Cyclic voltammograms of Co/N—C nanananotubes and Pt/C at a scan rate of 10 mV s^{-1} in O$_2$- or N$_2$-saturated 1 M KOH solutions. (b) Rotating disk electrode (RDE) linear sweep voltammograms of Co/N—C nanotubes and Pt/C at a rotation rate of 1600 rpm. (c) RDE voltammograms for Co/N—C nanotubes in O$_2$-saturated 1 M KOH solution at different rotation rates (scan rate 5 mV s^{-1}). (d) K—L plots of the ORR with Co/N—C nanotubes. (e) Tafel plots obtained from the RDE measurements at 1600 rpm. (f) Current—time chronoamperometric response of Co/N—C nanotubes and Pt/C in O$_2$-saturated 1 M KOH solution.

Table 1
Comparison of Co/N—C with other non-noble metal electrocatalysts for oxygen reduction reaction.

Catalyst	Mass loading (mg cm^{-2})	Onset potentials (V)	Tafel slope (mV dec^1)	Reference electrode	Reference
N, O, and S tridoped nanoporous carbons	0.203	0.96	60	*vs* RHE	[44]
Co@N-doped graphene	0.47	0.90	40	*vs* RHE	[30]
Co/N-CNT	0.2	0.94	50	*vs* RHE	[45]
Ni/N-CNTs	0.2	0.91	59	*vs* RHE	[45]
Fe—N—C	0.40	0.94	68	*vs* RHE	[46]
Fe—Cu @carbon	0.39	0.98	90	*vs* RHE	[47]
Fe$_3$C/C	0.60	1.05	59	*vs* RHE	[48]
Fe$_3$C/CNT	1.20	1.05	32	*vs* RHE	[49]
Co/N—C	**0.26**	**0.92**	**45.5**	***vs* RHE**	**This work**

excellent catalytic performance of Co/N—C catalyst could be attributed to the one-dimensional and internal void structure of Co/N—C samples, which facilitates fast electrolyte diffusion and electron transfer in ORR reaction. Besides, the increased content of Co nanoparticles embedded in carbon shells offers a great deal of ORR active sites. The increased coupling sites between Co nanoparticles and carbon shell could more effectively tune the work function and electron structure of carbon nanomaterials, thus leading to enhanced catalytic activity.

4. Conclusions

In summary, cobalt nanoparticles encapsulated in N-doped carbon nanotubes could be prepared by the in situ pyrolysis process. The obtained Co/N−C nanotubes possessing more than 50% void space allows for the free expansion of Co nanoparticles without mechanical constrain, and thus enhance the electrolyte diffusion rate. Furthermore, the increased content of Co nanoparticles in the electerode greatly improve the catalytic activity in ORR performance. As a result, it shows comparable electrocatalytic activity in alkaline electrolytes with commercial Pt/C, including a four electron transfer number, high current density, good durability capability, which makes it a promising candidate for ORR catalysts with effective and inexpensive non-platinum electrocatalysts in alkaline medium.

Conflict of interest

We declare that we have no conflict of interest.

Acknowledgements

References

[1] E.M. Erickson, M.S. Thorum, R. Vasic, N.S. Marinkovic, A.I. Frenkel, A.A. Gewirth, R.G. Nuzzo, J. Am. Chem. Soc. 134 (2012) 197−200.
[2] B.C.H. Steele, A. Heinzel, Nature 414 (2001) 345−352.
[3] S. Guo, S. Zhang, L. Wu, S. Sun, Angew. Chem. Int. Ed. 51 (2012), 11770−11173.
[4] M. Winter, R.J. Brodd, Chem. Rev. 104 (2004) 4245−4269.
[5] A.A. Gewirth, M.S. Thorum, Inorg. Chem. 49 (2010) 3557−3566.
[6] W. Xiong, F. Du, Y. Liu, A. Perez Jr., M. Supp, T.S. Ramakrishnan, L.M. Dai, L. Jiang, J. Am. Chem. Soc. 132 (2010) 15839−15841.
[7] Z.S. Wu, S. Yang, Y. Sun, K. Parvez, X. Feng, K. Muellen, J. Am. Chem. Soc. 134 (2012) 9082−9085.
[8] G. Wu, K.L. More, C.M. Johnston, P. Zelenay, Science 332 (2011) 443−447.
[9] Y.Y. Liang, Y.G. Li, H.L. Wang, J.G. Zhou, J. Wang, T. Regier, H.J. Dai, Nat. Mater 10 (2011) 780−786.
[10] M. Duerr, S. Gair, A.J. Cruden, J.R. McDonald, J. Power Sources 171 (2007) 1023−1032.
[11] L. Li, X. Feng, Y. Nie, S. Chen, F. Shi, K. Xiong, W. Ding, X. Qi, J. Hu, Z. Wei, L.J. Wan, M. Xia, ACS Catal. 5 (2015) 4825−4832.
[12] Y. Ma, R. Wang, H. Wang, J. Key, S. Ji, J. Power Sources 280 (2015) 526−535.
[13] R. Yang, K. Stevens, J.R. Dahn, J. Electrochem. Soc. 155 (2007) B79−B91.
[14] K. Huang, K. Bi, J.C. Xu, C. Liang, S. Lin, W.J. Wang, T.Z. Yang, Y.X. Du, R. Zhang, Electrochim. Acta 174 (2015) 172−177.
[15] B. Li, M. Zheng, H. Xue, H. Pang, Inorg. Chem. Front. 3 (2016) 175−202.
[16] C. Wei, Y. Liu, X. Li, J. Zhao, Z. Ren, Huan Pang, ChemElectroChem 1 (2014) 799−807.
[17] J. Zhao, C. Wei, H. Pang, Part. Part. Syst. Charact. 32 (2015) 429−433.
[18] Y. Tan, C. Xu, G. Chen, X. Fang, N. Zheng, Q. Xie, Adv. Funct. Mater 22 (2012) 4584−4591.
[19] Z. Wen, S. Ci, F. Zhang, X. Feng, S. Cui, S. Mao, S. Luo, Z. He, J. Chen, Adv. Mater 24 (2012) 1399−1404.
[20] J. Deng, P. Ren, D. Deng, X. Bao, Angew. Chem. Int. Ed. 54 (2015) 2100−2104.
[21] J. Deng, P.J. Ren, D.H. Deng, L. Yu, F. Yang, X.H. Bao, Energy Environ. Sci. 7 (2014) 1919−1923.
[22] X. Zou, X. Huang, A. Goswami, R. Silva, B.R. Sathe, E. Mikmekova, T. Asefa, Angew. Chem. Int. Ed. 53 (2014) 4372−4376.
[23] D. Deng, L. Yu, X. Chen, G. Wang, L. Jin, X. Pan, J. Deng, G. Sun, X. Bao, Angew. Chem. Int. Ed. 52 (2013) 371−375.
[24] J. Ren, M. Antonietti, T.-P. Fellinger, Adv. Energy Mater 5 (2015) 1401660−1401665.
[25] Y. Hou, Z. Wen, S. Cui, S. Ci, S. Mao, J. Chen, Adv. Funct. Mater 25 (2015) 872−882.
[26] W. Zhou, Y. Zhou, L. Yang, J. Huang, Y. Ke, K. Zhou, L. Lia, S. Chen, J. Mater. Chem. A 3 (2015) 1915−1919.
[27] W. Zhou, J. Zhou, Y. Zhou, J. Lu, K. Zhou, L. Yang, Z. Tang, L. Li, S. Chen, Chem. Mater 27 (2015) 2026−2032.
[28] Y. Zhao, J. Zhang, K. Li, Z. Ao, C. Wang, H. Liu, K. Sun, G. Wang, J. Mater. Chem. A 4 (2016) 12818−12824.
[29] A. Zhao, J. Masa, W. Xia, A. Maljusch, M.G. Willinger, G. Clavel, K. Xie, R. Schlögl, W. Schuhmann, M. Muhler, J. Am. Chem. Soc. 136 (2014) 7551−7554.
[30] M. Zeng, Y. Liu, F. Zhao, K. Nie, N. Han, X. Wang, W. Huang, X. Song, J. Zhong, Y. Li, Adv. Funct. Mater 26 (2016) 4397−4404.
[31] X. Zhang, R. Liu, Y. Zang, G. Liu, G. Wang, Y. Zhang, H. Zhang, H. Zhao, Chem. Commun. 52 (2016) 5946−5949.
[32] Y. Wang, Y. Nie, W. Ding, S.G. Chen, K. Xiong, X.Q. Qi, Y. Zhang, J. Wang, Z.D. Wei, Chem. Commun. 51 (2015) 8942−8945.
[33] D. Wang, F. Li, M. Liu, G. Lu, H. Cheng, Angew. Chem. Int. Ed. 47 (2008) 373−376.
[34] D.G. Lee, S.M. Kim, H. Jeong, J. Kim, I.S. Lee, ACS Nano 8 (2014) 4510−4521.
[35] H. Lee, S.M. Dellatore, W.M. Miller, P.B. Messersmith, Science 318 (2007) 426−430.
[36] M.J. Harrington, A. Masic, N.H. Andersen, J.H. Waite, P. Fratzl, Science 328 (2010) 216−220.
[37] D.R. Dreyer, D.J. Miller, B.D. Freeman, D.R. Paul, C.W. Bielawski, Langmuir 28 (2012) 6428−6435.
[38] J. Yang, M. Ma, C. Sun, Y. Zhang, W. Huang, X. Dong, J. Mater. Chem. A 3 (2015) 1258−1264.
[39] Y. Xia, X. Wang, W. Wang, D. Zhao, M. Cao, ACS Appl. Mater. Interfaces 6 (2014) 2051−2058.
[40] W. Jiao, N. Li, L.Z. Wang, L. Wen, F. Li, G. Liu, H.M. Cheng, Chem. Commun. 49 (2013) 3461−3463.
[41] A.M. El-Sawy, I.M. Mosa, D. Su, C.J. Guild, S. Khalid, R. Joesten, J.F. Rusling, S.L. Suib, Adv. Energy Mater 6 (2016) 1501966−1501977.
[42] Y.Z. Li, Z. Zhou, X.P. Gao, J. Yan, J. Power Sources 160 (2006) 633−637.
[43] S. Lee, H.J. Kim, S.M. Choi, M.H. Seo, W.B. Kim, Appl. Cat. A General 429−430 (2012) 39−47.
[44] Y. Meng, D. Voiry, A. Goswami, X. Zou, X. Huang, M. Chhowalla, Z. Liu, T. Asefa, J. Am. Chem. Soc. 136 (2014) 13554−13557.
[45] Y. Liu, H. Jiang, Y. Zhu, X. Yang, C. Li, J. Mater. Chem. A 4 (2016) 1694−1701.
[46] J. Liu, X. Sun, P. Song, Y. Zhang, W. Xing, W. Xu, Adv. Mater 25 (2013) 6879−6883.
[47] G. Nam, J. Park, M. Choi, P. Oh, S. Park, M.G. Kim, N. Park, J. Cho, J.S. Lee, ACS Nano 9 (2015) 6493−6501.
[48] Y. Hu, J.O. Jensen, W. Zhang, L.N. Cleemann, W. Xing, N.J. Bjerrum, Q. Li, Angew. Chem. Int. Ed. 53 (2014) 3675−3679.
[49] W. Yang, X. Yue, X. Liu, L. Chen, J. Jia, S. Guo, Nanoscale 8 (2016) 959−964.